Chinese Chemical Letters 32 (2021) 2143–2150

Contents lists available at ScienceDirect

Chinese Chemical Letters

journal homepage: www.elsevier.com/locate/cclet

Communication

# Porous $\alpha$-$Fe_2O_3$/$SnO_2$ nanoflower with enhanced sulfur selectivity and stability for $H_2S$ selective oxidation

Xiaohai Zheng, Jiaming Cai, Wentao Zhao, Shijing Liang*, Yong Zheng, Yanning Cao, Lijuan Shen*, Yihong Xiao, Lilong Jiang

*National Engineering Research Center of Chemical Fertilizer Catalyst, Fuzhou University, Fuzhou 350002, China*

ARTICLE INFO

*Article history:*
Received 31 July 2020
Received in revised form 21 September 2020
Accepted 8 November 2020
Available online 10 November 2020

*Keywords:*
Hierarchical structure
$Fe_2O_3$/$SnO_2$ composites
Oxygen vacancy
Synergistic effect
$H_2S$ selective oxidation

ABSTRACT

Being abundant and active, $Fe_2O_3$ is suitable for selective oxidation of $H_2S$. However, its practical application is limited due to the poor sulfur selectivity and rapid deactivation. Herein, we report a facile template-free hydrothermal method to fabricate porous $\alpha$-$Fe_2O_3$/$SnO_2$ composites with hierarchical nanoflower that can obviously improve the catalytic performance of $Fe_2O_3$. It was disclosed that the synergistic effect between $\alpha$-$Fe_2O_3$ and $SnO_2$ promotes the physico-chemical properties of $\alpha$-$Fe_2O_3$/$SnO_2$ composites. Specifically, the electron transfer between the $Fe^{2+}$/$Fe^{3+}$ and $Sn^{2+}$/$Sn^{4+}$ redox couples enhances the reducibility of $\alpha$-$Fe_2O_3$/$SnO_2$ composites. The number of oxygen vacancies is improved when the Fe cations incorporate into $SnO_2$ structure, which facilitates the adsorption and activation of oxygen species. Additionally, the porous structure improves the accessibility of $H_2S$ to active sites. Among the composites, Fe1Sn1 exhibits complete $H_2S$ conversion with 100% sulfur selectivity at 220 °C, better than those of pure $\alpha$-$Fe_2O_3$ and $SnO_2$. Moreover, Fe1Sn1 catalyst shows high stability and water resistance.



Hydrogen sulfide ($H_2S$), a highly toxic gas usually produced from coal mines, oil refineries, and sewage plants [1]. Hence, effective removal of $H_2S$ prior to emission is critical to pollution control and human safety. Industrially, $H_2S$ is mainly removed by the Claus technology [2,3]. However, about 4% of $H_2S$ is still left because of thermodynamic restriction. Among other advanced technologies, $H_2S$ selective oxidation process ($H_2S + 1/2O_2 \rightarrow S + H_2O$) appears to be the most promising candidate, because $H_2S$ could be wholly converted to elemental sulfur with low capital requirement [4]. Metal oxides, such as $TiO_2$ and $V_2O_5$, were applied in $H_2S$ selective oxidation. Nevertheless, $TiO_2$ is readily poisoned by $H_2O$ and the toxic nature of $V_2O_5$ is not desirable [5,6].

With natural abundance, favorable redox and nontoxic property, Fe-based materials are widely investigated in desulfurization [7]. Nevertheless, the excessive oxygen consumption of Fe-based materials leads to poor sulfur selectivity [8]. Additionally, rapid deactivation caused by the strong interaction between iron and sulfur severely impedes the practical application of iron-based catalysts. For instance, Mikenin *et al.* reported that the considerable $H_2S$ conversion of $FeO_x$-$SiO_2$/GFC catalyst is attributed to the high sulfur capacity of iron [9]. Zhang *et al.* investigated the catalytic performance of $Fe_2O_3$ modified semi-coke catalyst, which exhibited complete $H_2S$ conversion at 180 °C. Nevertheless, the stability was not satisfactory [10]. Various strategies have been proposed to address those issues, such as doping other metal components, decreasing the grain size of iron oxide and supported on carbon material with a large specific surface area [11]. The construction of composite oxide materials is an effective approach to improve the properties of iron oxide. Composite oxides can not only give play to the advantages of each component but also produce new properties that are not available in a single material due to the synergistic effect among components.

Tin oxide ($SnO_2$), as an n-type semiconductor, in which oxygen in the lattice can be easily migrated to the surface, providing a movable oxygen species to facilitate various reactions [12]. Lv *et al.* reported improved HCHO conversion over $Fe_2O_3$@$SnO_2$ composites compared with pure $Fe_2O_3$ and $SnO_2$, and related the enhanced activity to the synergetic effects of $Fe_2O_3$ and $SnO_2$ [13]. The Fe-Sn composite has been extensive studied in the field of electrocatalysis and photocatalysis due to its favorable properties caused by the synergetic effect of components [14,15]. Nonetheless, it is seldom to come across studies on the selective oxidation of $H_2S$. Considering the application of Fe-Sn composites in the $H_2S$ selective oxidation, the composites would give full play to the

* Corresponding authors.
*E-mail addresses:* jliang2011@gmail.com (S. Liang), syhgslj@fzu.edu.cn (L. Shen).

https://doi.org/10.1016/j.cclet.2020.11.017

advantages of pure $Fe_2O_3$ and $SnO_2$. Besides, it is possible for iron to enter the lattice of tin due to the radius of Fe ion is smaller than that of Sn ion, which would result in the adjustment of oxygen vacancy and reducibility. On the other hand, the lattice oxygen of $SnO_2$ is easily migrated to the surface to effectively convert $H_2S$ to S, which is beneficial to compensate for the low sulfur selectivity of iron oxide. Therefore, it is possible to take advantage of the properties of $Fe_2O_3$ and $SnO_2$ by constructing Fe-Sn composite material.

Toward this end, we fabricated a series of $\alpha$-$Fe_2O_3$/$SnO_2$ composites with hierarchical nanoflowers *via* a facile template-free hydrothermal process with the assistance of citric acid. The decomposition of citric acid during calcination would produce gases, which enables the formation of porous structures. This unique structure results in the $H_2S$ conversion, sulfur selectivity and durability of the obtained $\alpha$-$Fe_2O_3$/$SnO_2$ composites being superior to those of $\alpha$-$Fe_2O_3$ and $SnO_2$. We intrinsically clarified the effect of the interaction between Fe and Sn on the structures and physicochemical properties of the $\alpha$-$Fe_2O_3$/$SnO_2$ composites. In addition, the natures of active species and the reaction pathway are disclosed by the combination of the advanced characterizations.

The $\alpha$-$Fe_2O_3$/$SnO_2$ hierarchical nanostructures were prepared using a modified template-free hydrothermal strategy [16]. Typically, 1.5 g $Na_3C_6H_5O_7{\cdot}2H_2O$ and designated amount of $SnCl_4{\cdot}5H_2O$ were dissolved in distilled water (100 mL). Then the temperature was raised to 50 °C, followed by the addition of *x* mmol of $FeCl_3{\cdot}6H_2O$ and 1.92 g citric acid with further stirring for 30 min. After that, 50 mL of 6 wt% $NH_3{\cdot}H_2O$ solution was added dropwise into the above solution with vigorously stirred for 2 h. Subsequently, the obtained mixture was moved into a Teflon-sealed stainless steel autoclave and heated for 24 h at 100 °C. The precipitate was washed by distilled water and alcohol for 3 times before drying overnight at 85 °C. Finally, the hierarchical $\alpha$-$Fe_2O_3$/$SnO_2$ nanocomposites were harvested by calcined precipitates at 500 °C for 2 h in air (10 °C/min). The resulted catalysts are herein denoted as Fe*x*Sn*y* (where *x*:*y* = 1:2, 1:1 and 2:1; *x* + *y* = 0.06 mol).

Briefly, 6 g $C_2H_2O_4{\cdot}2H_2O$ was dissolved in 100 mL distilled water, and 12.12 g $Fe(NO_3)_3{\cdot}9H_2O$ was added to this solution with vigorous stirring for 2 h. The mixed solution was then sealed in a stainless-steel autoclave and heated for 24 h at 100 °C. After washing and drying at 85 °C overnight, the dark-red solid was calcined at 500 °C under an air flow for 2 h. The obtained catalyst was denoted as $\alpha$-$Fe_2O_3$.

Pure $SnO_2$ was prepared as follows [17]: 1.073 g $SnSO_4$ and 2.94 g $Na_2C_6H_5O_7{\cdot}2H_2O$ were dissolved in a mixed solution containing 15 mL ethyl alcohol and 60 mL distilled water, then the obtained solution was sealed to 100 mL autoclave and aged at 180 °C for 24 h. The precipitate was centrifuged and washed with alcohol and distilled water for 3 times. Finally, the product was dried at 100 °C for 12 h, then calcined at 500 °C for 2 h under an air flow.

The structural information of catalysts was studied using an X'Pert3 Pro instrument equipped with X-ray source of Cu K$\alpha$ (40 mA, 45 kV). $N_2$-sorption measurements were performed to explore the texture parameters of catalysts by employing a 3 Flex analyzer (U.S. Micromeritics). Scanning electron microscopy (SEM) images were given *via* Hitachi S-4800 electron microscope. Raman spectra were achieved on a Renishaw Viat Reflex spectrometer at room temperature ($\lambda$ = 532 nm). The concentrations of Fe and Sn were measured by inductively coupled plasma-atomic emission spectrometry (ICP-AES) analysis on a Perkin-Elmer Optima 8000 analyzer. Transmission electron microscopy (TEM) images were obtained by a JEM-2100F microscope (200 kV). Electron paramagnetic resonance (EPR) measurements were conducted at –196.5 °C by an EMX-8/2.7C X-band spectrometer (Bruker). X-ray photoelectron spectroscopy (XPS) data were recorded with a Thermo Escalab250 electron spectrometer equipped with a C 1s X-ray source (284.8 eV). UV–vis diffuse reflectance spectroscopy (UV–vis DRS) was performed on a Lambda 950 spectrophotometer using $BaSO_4$ as a reference. All the acquired spectra were transformed to Kubelka-Munk plots.

$H_2$-temperature programmed reduction ($H_2$-TPR) and $O_2$-temperature programmed desorption mass-spectrometry ($O_2$-

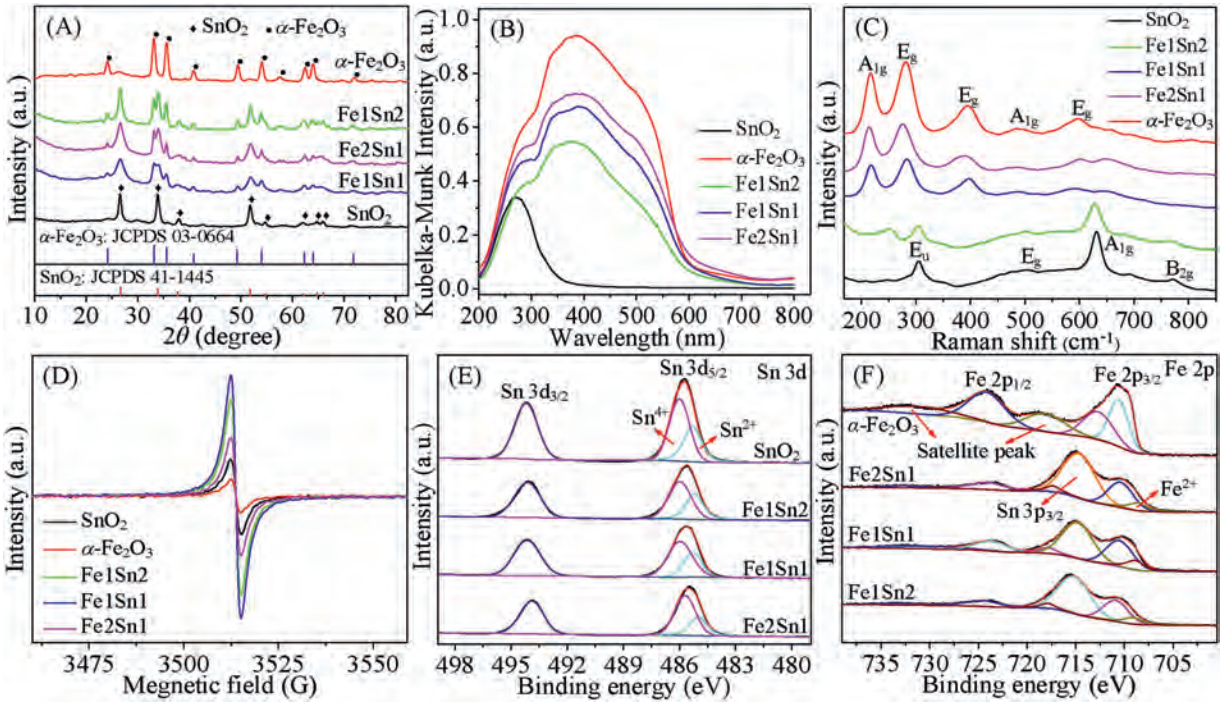


**Fig. 1.** (A) XRD pattern, (B) UV–vis DRS spectra, (C) Raman spectra, (D) EPR spectra, (E) XPS Sn 3d spectra, and (F) XPS Fe 2p spectra of as-synthesized $SnO_2$, $\alpha$-$Fe_2O_3$ and Fe*x*Sn*y* composites.

TPD-MS) profiles were performed in an AutoChem 2920 (Micromeritics) instrument equipped with a Hiden HPR-20 mass spectrometer. Prior to $H_2$-TPR experiment, the sample (0.1 g) was heated up to 300 °C in a He flow for 50 min (30 mL/min), and then cooled to 25 °C. The TPR data were collected by heating the samples at 50–900 °C (10 °C/min) in a 10 vol% $H_2$/Ar flow. Before $CO_2$-TPD-MS experiment, 0.1 g catalyst was heated in an Ar flow for 1 h at 300 °C and cooled to 25 °C. Then the $CO_2$ desorption profiles were recorded under Ar flow from 50 °C to 900 °C (10 °C/min). As for $O_2$-TPD-MS experiment, the pure $O_2$ gas was fed to the reactor at 25 °C for 1 h, and then $O_2$ profiles were recorded with the increase of temperature from 30 °C to 900 °C in a He flow.

$H_2S$ selective oxidation test of catalysts was performed in a fixed-bed reactor system from 100 °C to 250 °C (Fig. S1 in Supporting information). Typically, 0.2 g of catalyst (20 − 80 mesh) was taken into 8 mm round reactor. The reactant flow was composed of 2500 ppm $O_2$, 5000 ppm $H_2S$, 0–10 vol% $H_2O$, 0–500 ppm $SO_2$ and $N_2$ (balance gas). The total gas flow rate is 40 mL/min and the weight hourly space velocity (WHSV) is 12,000 mL $g^{-1}$ $h^{-1}$. The analysis of reactants and products were performed by a gas chromatograph with a TCD (thermal conductivity detector). A condenser was placed at the side of effluent to capture formed sulfur (S). The $H_2S$ conversion ($X_{H_2S}$), S selectivity ($S_{sulfur}$), and *S* yield were evaluated as follow:

$$X_{H_2S} = \frac{[H_2S]_{in} - [H_2S]_{out}}{[H_2S]_{in}} \times 100\% \quad (1)$$

$$S_{sulfur} = \frac{[H_2S]_{in} - [H_2S]_{out} - [SO_2]_{out}}{[H_2S]_{in} - [H_2S]_{out}} \times 100\% \quad (2)$$

$$\text{Sulfur yield} = [X_{H_2S}] \times [S_{sulfur}] \times 100\% \quad (3)$$

The turnover frequency (TOF, $s^{-1}$) was performed to compare the catalytic performance of obtained catalysts. The TOF values of $H_2S$ oxidation over Fe atoms were calculated using the equation:

$$\text{TOF} = \frac{(PCV_{gas}/RT \times X_{H_2S}}{\beta_{Fe} m_{cat.}/M_{Fe}} (s^{-1}) \quad (4)$$

Here, *R* means the proportional constant (8.314 J $mol^{-1}$ $K^{-1}$); *C*, *T* and *P* represent the $H_2S$ concentration, temperature (K) and standard atmospheric pressure ($1.01 \times 10^5$ Pa). $M_{Fe}$ and $\beta_{Fe}$ are the molar weight of Fe (55.85 g/mol) and Fe content (%). $V_{gas}$ and $m_{cat.}$ are the total molar flow rate (mol/s) and catalyst weight in grams.

The crystal structure of Fe*x*Sn*y* composites was determined by X-ray diffraction (XRD) analysis, and compared with those of $\alpha$-$Fe_2O_3$ and $SnO_2$. As presented in Fig. 1A, all the diffraction peaks for $SnO_2$ and $\alpha$-$Fe_2O_3$ are consistent with those of standard XRD patterns of tetragonal $SnO_2$ (JCPDS No. 41-1445, P42/MNM) and hexagonal $\alpha$-$Fe_2O_3$ (JCPDS No. 03-0664, R-3C) crystalline structures [18], respectively. As for Fe*x*Sn*y* composites, the strong peaks at $2\theta$ = 24.1°, 33.1°, 35.6°, 40.8°, 49.4°, 54.1°, 57.6°, 62.4°, 63.9° and 71.9° can be related to the (012), (104), (110), (113), (024), (116), (112), (214), (300) and (220) crystal planes of $\alpha$-$Fe_2O_3$. The distinct additional diffraction peaks at $2\theta$ = 26.7°, 33.7°, 37.8°, 51.7° and 65.9° are indexed to the (110), (101), (200), (211) and (301) crystal faces of $SnO_2$. It can be observed that (110) plane of Fe*x*Sn*y* composites slightly shifts to higher $2\theta$ value relative to pure $SnO_2$, which is caused by the lattice contraction due to the ionic size of $Fe^{3+}$ (0.064 nm) is smaller than $Sn^{4+}$ (0.071 nm) [19]. In addition, the diffraction peaks of Fe*x*Sn*y* composites show a decreasing intensity in comparison with those of $SnO_2$ and $\alpha$-$Fe_2O_3$, which could be due to a portion of $Fe^{3+}$ formed stable solid solutions with $SnO_2$. The Fe ions can occupy $SnO_2$ lattice sites, which leads to the change of stoichiometry and the introduction of point defects caused by charge imbalance [20]. Compared with the pure $SnO_2$, the diffraction peaks of $SnO_2$ over Fe*x*Sn*y* composites are broadened, indicating that the samples possess smaller crystal size (calculated values are shown in Table S1 (Supporting information).

The UV–vis DRS analysis was performed to investigate the nature of Sn and Fe species. As displayed in Fig. 1B, $SnO_2$ shows a band located at 275 nm, which could be ascribed to $Sn^{4+}$ and/or $Sn^{2+}$ species. The adsorption bands of $\alpha$-$Fe_2O_3$ could be divided into three subcurves at *ca.* 280, 390 and 500 nm. The band at 280 nm is assigned to isolated $Fe^{3+}$ species, and the bands at 390 nm and 500 nm are corresponding to oligonuclear $Fe^{3+}{}_xO_y$ complexes and larger $\alpha$-$Fe_2O_3$ nanoparticles [21]. As for Fe*x*Sn*y* composites, the band intensity of Fe*x*Sn*y* composites increases with increasing the mole ratio of iron, indicating the increase of iron species.

The vibrational and structural properties of catalysts are studied by Raman spectroscopy. It is accepted that $SnO_2$ possesses a rutile structure (tetragonal), which is ascribed to $D_{4h}{}^{14}$ space group. Therefore, $SnO_2$ should display eight Raman vibration modes ($\Gamma = A_{1g} + 2A_{2u} + A_{2g} + B_{1g} + 2B_{1u} + B_{2g} + 4E_u + E_g$) in the structure. Nevertheless, several modes including $A_{2u}$, $A_{2g}$, $B_{1u}$ and $B_{1g}$ are Raman silent [22]. As presented in Fig. 1C, the peaks of $SnO_2$ centered at *ca.* 305, 503, 632 and 778 $cm^{-1}$ are assigned to $E_u$, $E_g$, $A_{1g}$ and $B_{2g}$ vibration modes of rutile $SnO_2$ [23], respectively. $\alpha$-$Fe_2O_3$ shows five bands ($A_{1g}$, $E_g$, $E_g$, $A_{1g}$ and $E_g$) at 216, 282, 394, 483 and 597 $cm^{-1}$ [24]. For Fe*x*Sn*y* composites, they show peaks containing $\alpha$-$Fe_2O_3$ and $SnO_2$. It can be noticed that the peaks of $\alpha$-$Fe_2O_3$ dominate the Raman spectrum of Fe1Sn1 catalyst even for the mole ratio of Fe/Sn = 1 in the sample, which is attributed to the high intrinsic Raman spectrum intensity of $\alpha$-$Fe_2O_3$ in comparison to that of $SnO_2$ [25]. Compared with $SnO_2$, the Raman peaks of Fe*x*Sn*y* composites show a slight shift to lower wavenumber with the increase of iron content, mainly arising from the partial doping of Fe into $SnO_2$.

The EPR spectroscopy in Fig. 1D displays that the pristine $SnO_2$ exhibits one signal at g = 2.01, which is assigned to unpaired electrons trapped in singly ionized oxygen vacancies ($V_o$) [26]. The gaseous $O_2$ can be adsorbed on the vacancies and get electrons from the neighboring lattice $O^{2-}$ species to form electrophilic oxygen species ($O_2^-$ and $O_2^{2-}$) [27]. The EPR spectrum of $\alpha$-$Fe_2O_3$ shows an intense resonance signal at g = 2.03, which is assigned to the associates of Fe(III) ions [28]. As for Fe*x*Sn*y* composites, the signal intensity of oxygen vacancy shows an increase compared with pure $SnO_2$ and $\alpha$-$Fe_2O_3$, indicating the higher oxygen vacancy concentration of Fe*x*Sn*y* composites. Among them, Fe1Sn1 catalyst is the highest in the oxygen vacancy concentration. The above results indicate that the Fe cations incorporate into $SnO_2$ would increase the number of oxygen vacancies for the principle of electric neutrality. In addition, the $SnO_2$/$\alpha$-$Fe_2O_3$ composite would trigger the electron transfer from $SnO_2$ to $\alpha$-$Fe_2O_3$, which creates an electron accumulation layer on the side of $\alpha$-$Fe_2O_3$, leading to the adsorption and activation of more oxygen [29]. The oxygen vacancies and activated oxygen species present in the catalysts are critical for their catalytic performance.

The survey of XPS spectrum (Fig. S2 in Supporting information) indicates that Fe*x*Sn*y* composites are composed of elements including Sn, Fe and O (C is observed due to the C 1s (284.8 eV) was referenced to the calibration of binding energy). The Sn 3d XPS spectra of $SnO_2$ and Fe*x*Sn*y* composites are displayed in Fig. 1E. Clearly, there are two peaks centered at 485.7 eV and 494.2 eV, which are related to the spin-orbit splitting of Sn $3d_{5/2}$ and Sn $3d_{3/2}$, respectively. According to the NIST XPS database, the binding energy (BE) of $SnO_2$ ranged from 484.8 eV to 487.6 eV, and that of SnO ranged from 484.2 eV to 486.3 eV [30]. Thus, the peaks at

485.3 eV and 486.0 eV in the Sn $3d_{5/2}$ region are ascribed to $Sn^{2+}$ and $Sn^{4+}$ species, respectively. The relative percentages of $Sn^{2+}$ species in catalysts are listed in Table S1 (Supporting information), from which we observe that $SnO_2$ exhibits low $Sn^{2+}$ content (19.8%), while the Fe*x*Sn*y* composites display increased $Sn^{2+}$/($Sn^{2+}$ + $Sn^{4+}$) ratio. Because $Sn^{4+}$ is a scavenger of electrons and easily traps electrons, thus the electrons left by lattice O will combine with $Sn^{4+}$ to form $Sn^{2+}$.

As displayed in Fig. 1F, Fe 2p spectrum of $\alpha$-$Fe_2O_3$ gives two main peaks at 724.1 eV and 710.5 eV with two satellite peaks at 732.2 eV and 718.6 eV, which are ascribed to the spin-orbit splitting of Fe $2p_{1/2}$ and Fe $2p_{3/2}$, respectively. Fe*x*Sn*y* composites show an additional peak at BE of 715.6 eV that is assigned to Sn $3p_{3/2}$ [31]. Importantly, the energy difference between Fe $2p_{1/2}$ and Fe $2p_{3/2}$ (13.6 eV) are predominantly of $Fe^{3+}$. One additional peak at 709.1 eV is characteristic of $Fe^{2+}$, which is caused by the redox equilibrium $Sn^{2+} + 2Fe^{3+} \leftrightarrow Sn^{4+} + 2Fe^{2+}$. Note that the Fe 2p peak of Fe*x*Sn*y* composites shifts to lower BE in comparison with $\alpha$-$Fe_2O_3$, which may be attributed to electron redistribution of the Fe-Sn structure. As compiled in Table S1 (Supporting information), the Fe/(Fe + Sn) molar ratio over the samples increase with the rise of Fe content, in accordance with the ratios in the preparation of catalyst.

Fig. S3 (Supporting information) exhibits the XPS spectra in the O 1s region. There are two kinds of oxygen species located at 530.5 eV and 532.1 eV, which are ascribed to the lattice oxygen ($O_{Latt}$) and surface adsorbed oxygen ($O_{ads}$) [32]. Thus, the XPS spectra confirm the coexistence of lattice oxygen and oxygen vacancy within the $\alpha$-$Fe_2O_3$, $SnO_2$ and Fe*x*Sn*y* composites. The $O_{ads}$ species from oxygen vacancy is known to be more mobile than $O_{Latt}$, which is highly active in oxidation reactions [33]. The $O_{ads}$/($O_{ads}$ + $O_{Latt}$) ratios (Table S1) show that $O_{ads}$ species of Fe*x*Sn*y* composites are larger than pure $SnO_2$ and $\alpha$-$Fe_2O_3$, which achieves a maximum for the Fe1Sn1. The increase of $O_{ads}$ species over Fe*x*Sn*y* composites could be attributed to the unique properties of $SnO_2$: (i) $O_{ads}$ species in $SnO_2$ is active, and $O_{Latt}$ species is mobile, which results in the facile formation of oxygen vacancies. The active electrophilic $O_2^{2-}$ would be produced *via* the equation: $V_o + O_{2(gas)} + 2e- \leftrightarrow O_2^{2-} + 2h$ [34]. Then the active electrophilic $O_2^{2-}$ migrates to the surface of catalyst to form surface active oxygen; (ii) $SnO_2$ acts as a favorable promoter with strong oxygen transfer ability. When Fe enters into the $SnO_2$ lattice, the unstable lattice oxygen will transfer to the catalyst surface, which results in the formation of activated oxygen species [35]. Additionally, the binding energy of O 1s in Fe*x*Sn*y* composites is larger than that of pure $\alpha$-$Fe_2O_3$, which could be due to the electronegativity of Sn ($\chi$ = 1.96) is larger than that of Fe ($\chi$ = 1.83). Specifically, Sn possesses a stronger ability of capturing electrons than Fe, which causes the higher BE of O 1s in Fe*x*Sn*y* composites due to the smaller electron cloud density of oxygen [36].

The pore structure of $SnO_2$, $\alpha$-$Fe_2O_3$ and Fe*x*Sn*y* composites were investigated by $N_2$ adsorption-desorption experiments. As displayed in Fig. S4A (Supporting information), all the isotherms are typical IV type with type-H1 hysteresis loop in $P/P_0$ = 0.6–1.0, suggesting their mesoporous structure [37,38]. Fig. S4B (Supporting information) shows that all the pore sizes of samples fall within the mesoporous distribution. Table S2 lists the specific surface area, average pore diameter and pore volume calculated *via* $N_2$-sorption experiment. The specific surface area of $SnO_2$ and $\alpha$-$Fe_2O_3$ are 25.4 $m^2/g$ and 39.7 $m^2/g$, respectively. The Fe*x*Sn*y* composites show a larger specific surface area than pure $SnO_2$ and $\alpha$-$Fe_2O_3$. Among them, the Fe1Sn1 sample exhibits the largest specific surface area (55.6 $m^2/g$) and pore volume (0.33 $cm^3/g$), while that of Fe2Sn1 decreases slightly due to pore blockage resulted from the aggregation of excessive $Fe_2O_3$.

Figs. 2A–D exhibits the SEM images of the $SnO_2$ and Fe*x*Sn*y* composites, and all the catalysts show a flower-like 3D morphology with an average diameter of 2 μm. The flower-like architectures are comprised of a large number of short rods. The length of nanorods is 200–300 nm with a diameter of 80 nm. It can be seen that the rods of $SnO_2$ are loosely packed, and the rods of Fe*x*Sn*y* composites are piling up tighter with the rise of iron oxide content. The Fe2Sn1 catalyst shows some small particles, which could be caused by the formation of iron oxide particles. In addition, the $\alpha$-$Fe_2O_3$ possesses an irregular structure composed of nanoparticles (Fig. S5 in Supporting information). To get a closer observation of the growth processes for flower-like architectures, time-dependent studies were performed as shown in Fig. S6 (Supporting information). After 12 h reaction, the generated nanoparticles were elongated to form the rudiments of nanorods. Further prolonging the reaction time to 24 h, the hierarchical structures with a *ca.* 2 μm diameter were harvested. Based on the above results, the formation of hierarchical $\alpha$-$Fe_2O_3$/$SnO_2$ composites includes the generation of $SnO_2$ precursors, accompanied by a hydrolysis

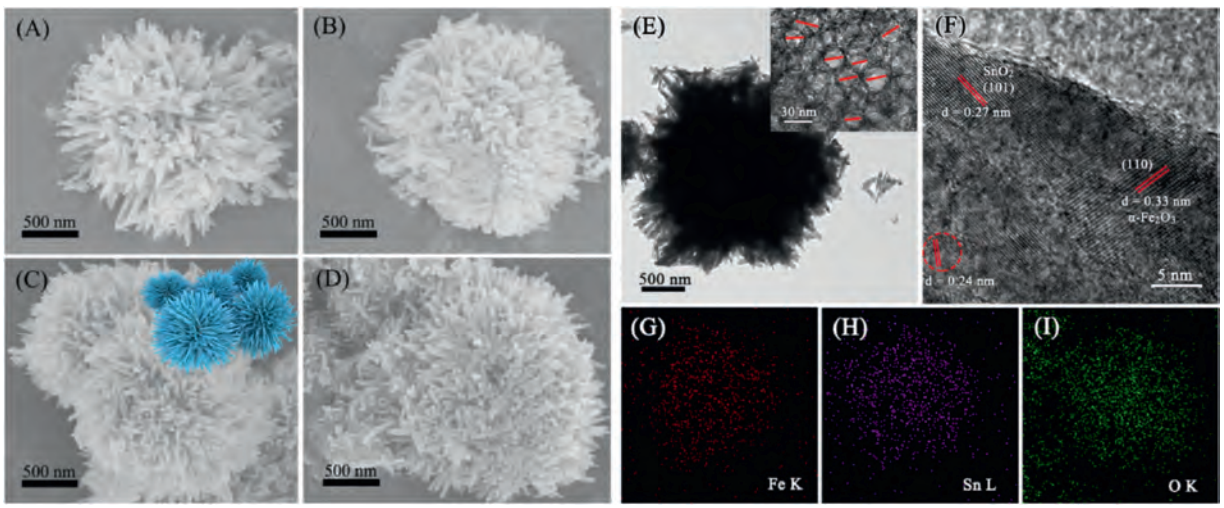


**Fig. 2.** SEM images of as-obtained catalysts: (A) $SnO_2$, (B) Fe1Sn2, (C) Fe1Sn1 and (D) Fe2Sn1; (E) TEM images, (F) HRTEM image, and (G–I) elemental mapping images of representative Fe1Sn1 catalyst.

process of $Fe^{3+}$ on the $SnO_2$ surface. The possible reaction pathway can be delineated as follow [39]:

$$Sn^{2+} \xrightarrow[\text{process}]{\text{oxidation}} Sn^{4+} \xrightarrow[\text{process}]{\text{hydrolysis}} Sn(OH)_6^{2-} \xrightarrow[\text{process}]{\text{decomposition}} SnO_2 \quad (5)$$

$$FeCl_3 + 2H_2O \xrightarrow[\text{process}]{\text{hydrolysis}} 3HCl + FeOOH \xrightarrow[\text{treatment}]{\text{thermal}} \alpha - Fe_2O_3 \quad (6)$$

As shown in Fig. 2E, Fe1Sn1 catalyst exhibits a sphere-like architecture that is assembled by short-rods, in consistent with the SEM results. An inset TEM image shows that Fe1Sn1 possesses a porous structure, and its average pore diameter is *ca.* 24.7 nm, which coincides with the BET results. The HRTEM image in Fig. 2F shows that the fringe spacings of 0.27 nm and 0.33 nm match well with the (101) plane of $SnO_2$ and (110) plane of $\alpha$-$Fe_2O_3$, which are dovetail with the XRD spectra at $2\theta = 33.9°$ and 35.6°. There is not a clear interface between these two nanocrystals, indicating that the Fe*x*Sn*y* composites are not heterojunction structures. In addition, new lattice fringe of 0.24 nm appear in the HRTEM image of Fe1Sn1, this distorted lattice lines (marked by a dotted box) may be attributed to the incorporation of partial Fe atoms into $SnO_2$ lattices, leading to the decrease of the lattice spacing or the formation of solid solutions [40]. The elemental mapping images presented in Figs. 2G–I suggest that the elements Fe, Sn and O are uniformly distributed throughout the whole nanoflower.

The influence of reaction temperature on the $H_2S$ conversion of $SnO_2$, $\alpha$-$Fe_2O_3$ and Fe*x*Sn*y* composites are displayed in Fig. 3A. The $H_2S$ conversion over $SnO_2$ is only 19% at 100 °C, and it is increased to 74% at 250 °C. The $H_2S$ conversion of $\alpha$-$Fe_2O_3$ increases from 41% to 100% with the reaction temperature rises from 100 °C to 250 °C. For Fe1Sn2 and Fe2Sn1, the $H_2S$ conversion initially increases with the rise of temperature up to 220 °C, and then remains constant at about 100%. The results indicate that the catalytic activity of Fe*x*Sn*y* composites is higher than those of $SnO_2$ and $\alpha$-$Fe_2O_3$. Among them, Fe1Sn1 exhibits the highest $H_2S$ conversion over the entire reaction temperature range, which is higher than reported Fe-based catalysts for the $H_2S$ selective oxidation (Table S3 in Supporting information).

Figs. 3B and C depict the sulfur selectivity and sulfur yield as a function of temperature. When the reaction temperature is below 130 °C, the sulfur selectivity of all samples is 100%. As the temperature increases, the sulfur selectivity of $\alpha$-$Fe_2O_3$ and Fe2Sn1 decreases. When the reaction temperature increases to 160 °C, the sulfur selectivity of $SnO_2$, Fe1Sn1 and Fe1Sn2 samples also decreases. This could be attributed to side reactions, including $H_2S$ deep oxidation ($H_2S + 3/2O_2 \rightarrow H_2O + SO_2$) and sulfur oxidation ($S + O_2 \rightarrow SO_2$) [41]. The sulfur selectivity of Fe1Sn1 sample decreases slowly compared with other samples, and shows relatively good sulfur selectivity within the reaction temperature range. Even at the reaction temperature of 250 °C, it is sulfur selectivity (92.1%) is still higher than that of other samples. As shown in Fig. 3C, similar to $H_2S$ conversion, the sulfur yield of samples firstly rises with the increase of reaction temperature (100–220 °C). As the temperature further increasing to 250 °C, the sulfur yield of $SnO_2$ and Fe1Sn2 increases, while that of $\alpha$-$Fe_2O_3$, Fe1Sn1 and Fe2Sn1 decreases. This is attributed to a decrease in sulfur selectivity. Overall, the Fe*x*Sn*y* composites exhibit higher $H_2S$ conversion than that of $\alpha$-$Fe_2O_3$ and $SnO_2$. The sulfur has been recovered from condenser (Fig. S7 in Supporting information). In addition, an analysis of sulfur mass balance on the basis of sulfur in the used catalyst and recovered S was conducted, and the calculated data is close to the S yield.

To more closely get insight into the intrinsic reactivity of as-synthesized catalysts, the reaction rates under WHSV = 36,000 mL $g^{-1}$ $h^{-1}$ ($H_2S$ conversion is below 20% in order to eliminate external/internal diffusion effects) were calculated using the formula: $r_{H_2S} = \frac{X_{H_2S} \times C \times V_{gas}}{m_{cat.}}$ (mol $g_{cat}^{-1}$ $s^{-1}$), where $X_{H_2S}$ is the $H_2S$ conversion, $m_{cat.}$ represents the catalyst weight in gram, $C$ and $V_{gas}$ are the $H_2S$ concentration and total molar flow rate of inlet gases. The corresponding activation energies ($E_a$) were calculated *via* Arrhenius plots (Fig. 3D), the results are compiled in Table S4 (Supporting information). The superiority of Fe*x*Sn*y* composites as

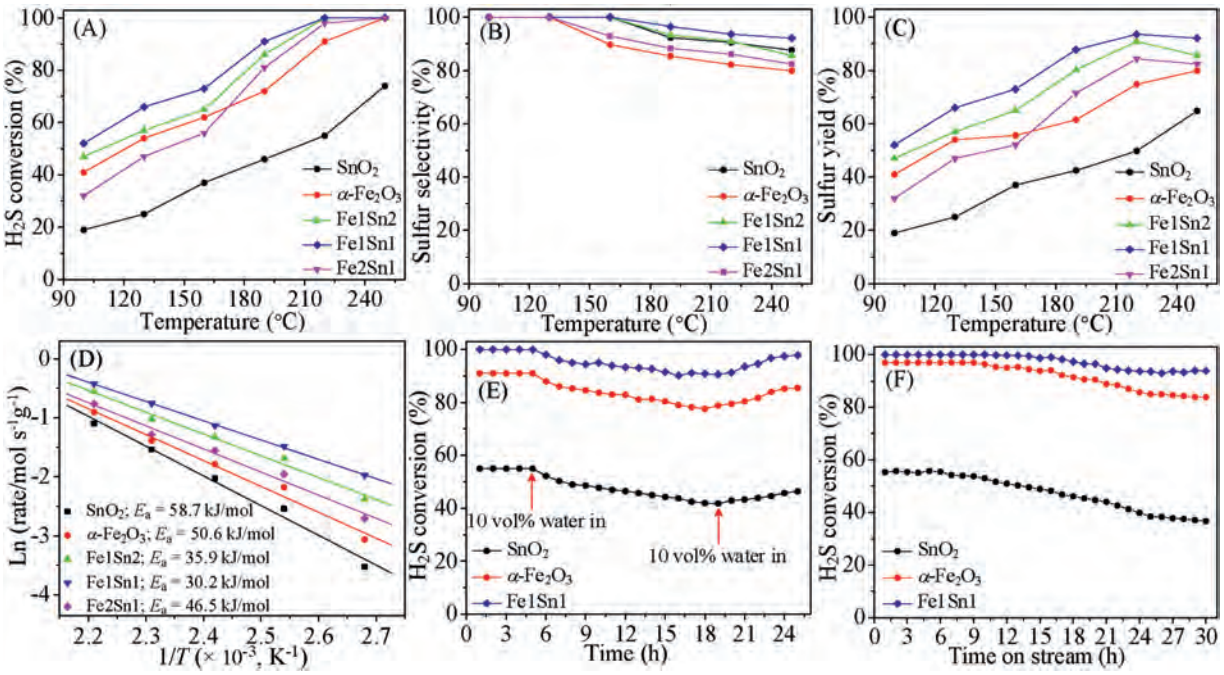


**Fig. 3.** (A) $H_2S$ conversion, (B) sulfur selectivity, (C) sulfur yield, and (D) Arrhenius plots for $H_2S$ oxidation over the $SnO_2$, $\alpha$-$Fe_2O_3$ and Fe*x*Sn*y* composites. (E) 10 vol% $H_2O$ tolerance test of the $SnO_2$, $\alpha$-$Fe_2O_3$ and Fe1Sn1 catalyst. (F) Stability test of the $SnO_2$, $\alpha$-$Fe_2O_3$ and Fe1Sn1 catalyst at 220 °C.

compared to pure $SnO_2$ and $\alpha$-$Fe_2O_3$ is obvious, clearly demonstrating the synergistic Fe-Sn interactions. It can be seen that the Fe1Sn1 catalyst exhibits the highest reaction rate ($4.47 \times 10^{-7}$ mol $g_{cat.}^{-1}$ $s^{-1}$), followed by Fe1Sn2 ($3.89 \times 10^{-7}$ mol $g_{cat.}^{-1}$ $s^{-1}$), Fe2Sn1 ($3.14 \times 10^{-7}$ mol $g_{cat.}^{-1}$ $s^{-1}$), $\alpha$-$Fe_2O_3$ ($2.36 \times 10^{-7}$ mol $g_{cat.}^{-1}$ $s^{-1}$), and $SnO_2$ ($1.31 \times 10^{-7}$ mol $g_{cat.}^{-1}$ $s^{-1}$), a trend identical to $H_2S$ conversion. In relation to the activation energies, Fe1Sn1 shows the lowest activation energy (30.2 kJ/mol) among Fe*x*Sn*y* composites, followed by Fe1Sn2 and Fe2Sn1. On the other hand, the pure $SnO_2$ exhibits the highest activation energy, implying a higher energy barrier for $H_2S$ oxidation over pure $SnO_2$. Additionally, the TOF values over $H_2S$ selective oxidation based on Fe species were calculated and summarized in Table S4. Similar to the $H_2S$ conversion results, the TOFs over as-obtained catalysts follows the trend: Fe1Sn1 > Fe1Sn2 > Fe2Sn1 > $\alpha$-$Fe_2O_3$ > $SnO_2$. The results of intrinsic reactivity indicate that $H_2S$ conversion is strongly dependent on the mole ratio of Fe/Sn.

Sulfur-containing streams in industry usually contain a certain amount of water vapor. Thus, it is crucial to investigate the effect of $H_2O$ on the $H_2S$ selective oxidation over $SnO_2$, $\alpha$-$Fe_2O_3$, and Fe1Sn1 at 220 °C. As illustrated in Fig. 3E, $H_2S$ conversion of Fe1Sn1 decreases from 100% to 90.2% and remains stable after the introduction of 10 vol% $H_2O$. As for $\alpha$-$Fe_2O_3$ and $SnO_2$, the $H_2S$ conversion decreases to 77.6% and 41.8% after the addition of $H_2O$, respectively. The partial decrease of catalytic activity could be related to the competing adsorption of $H_2O$ and $H_2S$ on the same active sites [42]. Additionally, the introduction of $H_2O$ causes the reverse Claus reaction ($3S + 2H_2O \leftrightarrow 2H_2S + SO_2$), which also results in the decline of catalytic activity for $H_2S$ oxidation. With the stop of $H_2O$ supply, the $H_2S$ conversion of Fe1Sn1 recovers to *ca.* 97.8%, higher than that of $\alpha$-$Fe_2O_3$ (85.5%) and $SnO_2$ (46.4%). Overall, the Fe1Sn shows a high tolerance of $H_2O$ for the reaction of $H_2S$ oxidation.

The stability test over Fe1Sn1 catalyst is depicted in Fig. 3F. The $H_2S$ conversion of $SnO_2$ catalyst is maintained at 55% for the first 6 h, after which the $H_2S$ conversion gradually decreases to only 36% after 30 h reaction. For $\alpha$-$Fe_2O_3$ catalyst, the $H_2S$ conversion keeps at ~ 97% in the initial 9 h, then decreases with the extension of time. After 30 h reaction, the $H_2S$ conversion of $\alpha$-$Fe_2O_3$ is 83%. The low stability of pure $SnO_2$ and $\alpha$-$Fe_2O_3$ is attributed to the deposition of sulfate and sulfur during reaction [43]. As for the Fe1Sn1 catalyst, the $H_2S$ conversion remains *ca.* 100% within 16 h, then it decreases slightly and remains constant at 94%. We can inferred that the higher concentration of oxygen vacancies in Fe1Sn1 would promote the $O_2$ activation and hinder the formation of byproducts, ultimately leads to the higher stability of Fe1Sn1. Additionally, the porous structure facilitates the desorption of elemental sulfur and by-product $SO_2$. After stability test, $\alpha$-$Fe_2O_3$ displays an irregular structure composed of nanoparticles (Fig. S8 in Supporting information). As for $SnO_2$, it shows a slight change in comparison with the fresh one. It can be seen that the as-prepared Fe1Sn1 catalyst maintains the original morphology after stability test, indicating the structure stability of Fe1Sn1.

To explore the impact of WHSV on the catalytic activity of Fe1Sn1, a series of tests were performed at WHSV = 9000–15,000 mL $g^{-1}$ $h^{-1}$. As displayed in Fig. S9A (Supporting information), Fe1Sn1 shows *ca.* 100% $H_2S$ conversion at WHSV below 12,000 mL $g^{-1}$ $h^{-1}$. Subsequently, a further rise of WHSV causes a decline of $H_2S$ conversion (90% at 15,000 mL $g^{-1}$ $h^{-1}$). Besides, sulfur selectivity shows a gradual decline in a WHSV range of 9000–15,000 mL $g^{-1}$ $h^{-1}$. Though the sulfur yield decreases at higher WHSV, it is still larger than 80% because of the relatively high sulfur selectivity. Fig. S9B (Supporting information) presents the effect of $H_2S/O_2$ molar ratio on activities over Fe1Sn1 catalyst for $H_2S$ oxidation conducted at 220 °C. Fe1Sn1 displays nearly 95% $H_2S$ conversion and 94% S selectivity at $H_2S/O_2 = 3$. When $H_2S/O_2 = 2$, $H_2S$ conversion increases to *ca.* 100% and S selectivity remains at 94%. Moreover, $H_2S$ conversion keeps close to 100%, while sulfur selectivity decrease to 86% with the $H_2S/O_2$ molar ratio decreases to 1:2. These results indicate that excessive oxygen is in favor of $H_2S$ deep oxidation, whereas insufficient oxygen causes the low $H_2S$ conversion [44].

To gain information about redox chemistry of the catalysts, $H_2$-TPR measurements were carried out and the monitored TCD signals are delineated in Fig. 4A. Pure $SnO_2$ shows a reduction peak at 645 °C, which is related to the reduction of $SnO_2$ to Sn metal [45]. For pure iron oxide, the peaks at 510 °C and 590 °C correspond to the reduction of $Fe_2O_3 \rightarrow FeO$ and $FeO \rightarrow Fe$ [46], respectively. As for Fe*x*Sn*y* composites, Fe1Sn2 catalyst exhibits two strong peaks at 340 °C and 635 °C. The former peak is related to the reduction of $Fe_2O_3 \rightarrow FeO$, and the latter peak is assigned to concurrent reduction of FeO and $SnO_2$ into respective metals. The reduction peaks of Fe1Sn1 catalyst shift to lower temperatures in comparison with pure $SnO_2$, $\alpha$-$Fe_2O_3$ and other Fe*x*Sn*y* composites, which indicates that the strong interaction between $Fe^{3+}/Fe^{2+}$ and $Sn^{4+}/Sn^{2+}$ through the redox equilibrium of $Sn^{2+} + 2Fe^{3+} \leftrightarrow Sn^{4+} + 2Fe^{2+}$, suggesting that the oxygen atoms of the Fe1Sn1 catalyst are easier to migrate to generate oxygen vacancy during the reduction process [47]. The strong interaction also makes both $Fe^{3+}$ and $Sn^{4+}$ become more reducible. In addition, the amount of $H_2$ consumption (Table S5 in Supporting information) and initial $H_2$ consumption rate (Fig. 4B) derived from $H_2$-TPR profiles also confirm that the Fe1Sn1 possesses the highest $H_2$ consumption and initial $H_2$ consumption rate. The above results indicate that the Fe*x*Sn*y* composites (especially Fe1Sn1) show higher redox properties, which is beneficial for $H_2S$ oxidation.

$O_2$ activation is an important factor in oxidation reactions, thus $O_2$-TPD-MS was measured to characterize the nature of surface oxygen species. As shown in Fig. 4C, $SnO_2$ sample exhibits two peaks centered at 520 °C and 710 °C, which are related to the decomposition of chemically adsorbed $O^{2-}$ ($O_{ads}$) and lattice $O^{2-}$ ($O_{latt}$) [48], respectively. The TPD profile of $\alpha$-$Fe_2O_3$ also appears

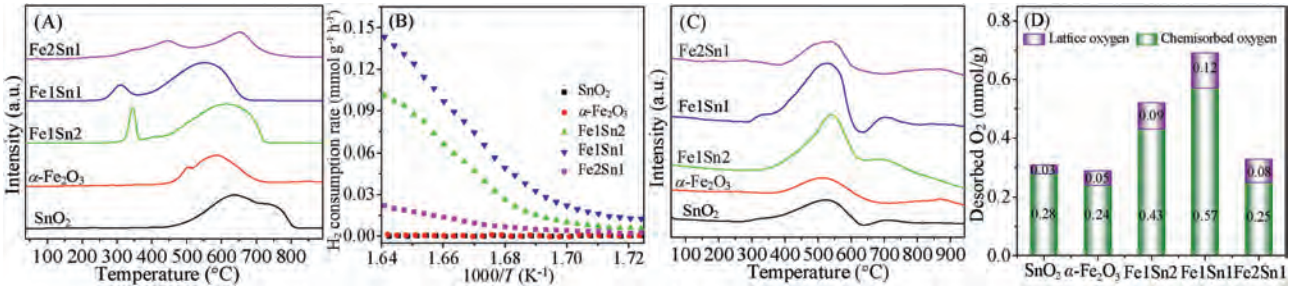


**Fig. 4.** (A) $H_2$-TPR profiles, (B) initial $H_2$ consumption rate, (C) $O_2$-TPD-MS profiles and (D) the amount of desorbed $O_2$ over $SnO_2$, $\alpha$-$Fe_2O_3$ and Fe*x*Sn*y* composites.

two desorption peaks at 501 °C and 860 °C corresponding to $O_{ads}$ and $O_{latt}$ species. As for Fe*x*Sn*y* composites, the peak intensity of $O_{ads}$ over Fe1Sn1 catalyst is higher than that of Fe2Sn1 and Fe1Sn2, which indicates that Fe1Sn1 catalyst possesses higher chemisorbed oxygen species. The enhancement of surface oxygen species could be released base on the equations: $Fe^{2+}$-$V_o$-$Sn^{2+}$ + $2O_2$ ↔ $Fe^{2+}$-$2O_2^-$-$Sn^{4+}$, $Fe^{2+}$-$2O_2^-$-$Sn^{4+}$ + $O_2$ ↔ $Fe^{3+}$-$3O_2^-$-$Sn^{4+}$. Additionally, $SnO_2$ can effectively convert adsorbed oxygen to $O^{2-}$ because of improved electron transfer performance of chemically adsorbed oxygen on the $SnO_2$ surface. Noted that the lower desorption temperatures of the Fe1Sn1 are induced by the weaker bonding energy between the oxygen vacancies and adsorbed oxygen, which could result in better oxygen mobility. The amount of desorbed oxygen derived from $O_2$-TPD-MS profiles (Fig. 4D and Table S6 in Supporting information) also confirms that the Fe1Sn1 catalyst exhibits the largest amount of available oxygen, which is accordance with the result of catalytic activities.

According to the results of $H_2$-TPR and $O_2$-TPD-MS measurements, it is concluded that the oxygen vacancies can be formed when the Fe cations incorporate into the $SnO_2$ for the principle of electric neutrality. The oxygen vacancies in the Fe-Sn composites favors for the $O_2$ adsorption and activation of oxygen species. In addition, the electron transfer between the $Fe^{2+}/Fe^{3+}$ and $Sn^{2+}/Sn^{4+}$ redox couples enhances the reducibility of Fe-Sn composites. Overall, the enrichment of active oxygen species and enhancement of reducibility improve catalytic performance toward $H_2S$ oxidation.

For detailed investigation of the chemistry status variation during the reaction, the XPS was conducted. As displayed in Fig. S10A (Supporting information), the Fe 2p spectra of fresh and used Fe1Sn1 catalyst indicate that the Fe species is still in a state of $Fe^{3+}/Fe^{2+}$ mixed valence. Besides, the peak intensity of $Fe^{2+}$ increases after reaction (the molar ratio of $Fe^{2+}/Fe^{3+}$ increases from 8.7%–13.5%), which is attributed to the Fe diffusion from bulk to the surface [49]. As displayed in Fig. S10B (Supporting information), the Sn 3d spectrum of used Fe1Sn1 is similar to the fresh one, except for the decrease intensity of $Sn^{2+}$ peak (the molar ratio of $Sn^{2+}/Sn^{4+}$ decreases from 28.3%–23.5% after reaction). The variation of $Fe^{2+}/Fe^{3+}$ and $Sn^{2+}/Sn^{4+}$ during the reaction demonstrates the electron transfer between the $Fe^{2+}/Fe^{3+}$ and $Sn^{2+}/Sn^{4+}$ redox couples, which also indicates the participation of $Fe^{2+}/Fe^{3+}$ and $Sn^{2+}/Sn^{4+}$ species in the reaction. As reported by Lu *et al.*, the adsorbed $O_2$ transforms into dissociated oxygen species by electron transfer, which occurs more easily on the surface of reduced $SnO_{2-x}$ than perfect $SnO_2$ [50]. Therefore, the presence of $Sn^{2+}$ cations on the $SnO_2$ surface facilitates the catalytic activity. The O 1s spectra (Fig. S10C in Supporting information) imply that there is a decline of the $O_{ads}$ after the reaction, which confirms the participation of chemisorbed oxygen and lattice oxygen species in $H_2S$ selective oxidation.

The deposition of elemental sulfur and sulfate could be corroborated by XPS analysis. As shown in Fig. S10D (Supporting information), no S 2p signal is found in the fresh catalyst while the used one shows two discernible components relating to different sulfur species are observed at 163.5 eV and 168.2 eV, which are ascribed to the presence of S and $SO_4^{2-}$ species [51]. The XRD pattern (Fig. S11 in Supporting information) of the used Fe1Sn1 sample remains all the peaks of the fresh one, indicating that the structure of Fe1Sn1 could be sustained during the desulfurization process. Meanwhile, a new peak at $2\theta = 22.4^\circ$ assigned to sulfur is found, confirming the formation of S during the reaction [52].

According to the above analysis, we propose that the plausible reaction pathway of $H_2S$ oxidation over the as-prepared $\alpha$-$Fe_2O_3$/$SnO_2$ nanocomposite is as follows (Fig. S12 in Supporting information). $H_2S$ molecules first adsorb on the Fe sites due to Fe ($\chi = 1.83$) is less electronegative than Sn ($\chi = 1.96$) [53]. Subsequently, the dissociated adsorbed $H_2S$ is oxidized into sulfur by surface adsorbed oxygen and activated lattice oxygen. Meanwhile, the consumed oxygen's neighboring surface $Fe^{3+}$ and $Sn^{4+}$ cations are reduced to $Fe^{2+}$ and $Sn^{2+}$. Finally, the consumed oxygen will be replenished by the gaseous $O_2$ ($O_{2(g)}$ + $V_o$ → $2O_{(ads)}$) with the formation of $Fe^{3+}$ and $Sn^{4+}$ to complete the reaction cycle [54]. Note that the electron transfer between the $Fe^{2+}/Fe^{3+}$ and $Sn^{2+}/Sn^{4+}$ redox couples can enhance the activation of oxygen in the catalyst. Moreover, the favorable catalytic activity and durability of the $\alpha$-$Fe_2O_3$/$SnO_2$ nanostructures are due mainly to the enhanced reducibility, abundant oxygen vacancies and strong interaction between the $\alpha$-$Fe_2O_3$ and $SnO_2$ phases over the catalyst. In addition, the porous structure facilitates the adsorption and diffusion of reactants, which also contributes to the high catalytic performance.

In summary, a series of porous $\alpha$-$Fe_2O_3$/$SnO_2$ nanostructures were synthesized by regulating the Fe/Sn molar ratio. The influence of the Fe/Sn molar ratio and chemical states of Fe and Sn on the active oxygen concentration and catalytic performance of $\alpha$-$Fe_2O_3$/$SnO_2$ nanostructures was investigated. The synergy between $Fe_2O_3$ and $SnO_2$ leads to a higher concentration of oxygen vacancy, active oxygen species and enhanced redox properties. In addition, the constructed porous structure facilitates favorable mass transport during the reaction process. As a consequence, Fe1Sn1 catalyst is the most excellent among $SnO_2$, $\alpha$-$Fe_2O_3$ and Fe*x*Sn*y* composites, showing complete $H_2S$ conversion and 100% S selectivity at 220 °C, superior to those of individual $\alpha$-$Fe_2O_3$ and $SnO_2$. More importantly, Fe1Sn1 catalyst shows high stability and water resistance. We can rationally anticipate that the porous $\alpha$-$Fe_2O_3$/$SnO_2$ nanocomposite is an efficient and promising catalyst for the oxidative desulphurization reaction.

## Declaration of competing interest

The authors report no declarations of interest.

## Acknowledgments

This work was supported by the National Natural Science Fund for Distinguished Young Scholars of China (No. 21825801), National Natural Science Foundation of China (Nos.21677036, 21878052 and 21773030).

## Appendix A. Supplementary data

Supplementary material related to this article can be found, in the online version, at doi:https://doi.org/10.1016/j.cclet.2020.11.017.

## References

[1] P. Ding, D. Xu, N. Dong, et al., Chin. Chem. Lett. 31 (2020) 2050–2054.
[2] C. Lei, W. Zhou, L. Shen, et al., ACS Sustainable Chem. Eng. 7 (2019) 16257–16263.
[3] Y. Cao, X. Zheng, Z. Du, et al., Ind. Eng. Chem. Res. 58 (2019) 19353–19360.
[4] Y. Pan, M. Chen, M. Hu, et al., Appl. Catal. B: Environ. 262 (2019) 118266.
[5] K.V. Bineesh, D.K. Kim, M.I. Kim, D.W. Park, Appl. Clay Sci. 53 (2011) 204–211.
[6] X. Zhang, G. Dou, Z. Wang, et al., Catal. Sci. Technol. 3 (2013) 2778–2785.
[7] K.V. Bineesh, D.K. Kim, M.I. Kim, et al., Dalton Trans. 40 (2011) 3938–3945.
[8] F. Zhang, X. Zhang, G. Jiang, et al., Chem. Eng. J. 348 (2018) 831–839.
[9] P. Mikenin, S. Zazhigalov, A. Elyshev, et al., Catal. Commun. 87 (2016) 36–40.
[10] X.Y. Zhang, L. Cui, D.H. An, et al., Energy Fuels 34 (2020) 2315–2322.
[11] W. Zhao, X. Zheng, S. Liang, et al., Green Chem. 20 (2018) 4645–4654.
[12] Z. Zhao, B. Wang, J. Ma, et al., Chinese J. Catal. 38 (2017) 1322–1329.
[13] T. Lv, C. Peng, H. Zhu, W. Xiao, Appl. Surf. Sci. 457 (2018) 83–92.
[14] C. Zhao, W. Hu, Z. Zhang, et al., Sens. Actuat. B: Chem. 195 (2014) 486–493.
[15] M. Niu, F. Huang, L. Cui, et al., ACS Nano 4 (2010) 681–688.
[16] X.Y. Liu, Y.L. Han, Q. Li, D. Pan, Key Eng. Mater. 727 (2017) 718–725.
[17] P. Sun, W. Zhao, Y. Cao, et al., Cryst. Eng. Comm. 13 (2011) 3718–3724.
[18] Y. Yin, S. Xin, L. Wan, et al., Sci. China Chem. 55 (2012) 1314–1318.

[19] M.M. Bagheri-Mohagheghi, N. Shahtahmasebi, M.R. Alinejad, et al., Solid State Sci. 11 (2009) 233–239.
[20] L. Fang, X. Zu, Z. Li, et al., J. Alloys. Compd. 454 (2008) 261–267.
[21] X. Zhang, G. Dou, Z. Wang, et al., J. Hazard. Mater. 260 (2013) 104–111.
[22] V. Bonu, A. Das, A. Sivadasan, et al., J. Raman Spectrosc. 46 (2015) 1037–1040.
[23] Y. Yan, F.H. Du, X.P. Shen, et al., J. Mater. Chem. A Mater. Energy Sustain. 2 (2014) 15875–15882.
[24] H. Liang, C. Xia, A.H. Emwas, et al., Nano Energy 49 (2018) 155–162.
[25] M. Rumyantseva, V. Kovalenko, A. Gaskov, et al., Sens. Actuat. B: Chem. 109 (2005) 64–74.
[26] M. D'Arienzo, D. Cristofori, R. Scotti, F. Morazzoni, Chem. Mater. 25 (2013) 3675–3686.
[27] J.W. Xu, Y. Zhang, X.L. Xu, et al., ACS Catal. 9 (2019) 4030–4045.
[28] H. Mahmoud, I. Battisha, F. Ezz-Eldin, Spectrochim. Acta A 150 (2015) 72–82.
[29] Y. Guo, J. Liang, Y. Liu, et al., Ind. Eng. Chem. Res. 58 (2019) 18569–18581.
[30] S. Chai, X. Bai, J. Li, et al., Appl. Surf. Sci. 402 (2017) 12–20.
[31] N. Wang, Y. Du, W. Ma, et al., Appl. Catal. B: Environ. 210 (2017) 23–33.
[32] P. Wang, Y. Ji, Q. Shao, et al., Sci. Bull. (Beijing) 65 (2019) 350–358.
[33] H. Liu, Y. Wu, L. Liu, et al., Appl. Surf. Sci. 498 (2019) 143780.
[34] Y. Liu, Y. Liu, Y. Guo, et al., Ind. Eng. Chem. Res. 57 (2018) 14052–14063.
[35] J.Y. Liu, M.J. Dai, T.S. Wang, et al., ACS Appl. Mater. Interfaces 8 (2016) 6669–6677.
[36] X. Yao, Y. Xiong, W. Zou, et al., Appl. Catal. B: Environ. 144 (2014) 152–165.
[37] X. Zheng, X. Chen, J. Chen, et al., Chem. Eng. J. 297 (2016) 148–157.
[38] Y. Xiao, X. Zheng, X. Chen, et al., Ind. Eng. Chem. Res. 56 (2017) 1687–1695.
[39] P. Sun, Y. Cai, S. Du, et al., Sens. Actuat. B: Chem. 182 (2013) 336–343.
[40] H. Kanai, H. Mizutani, T. Tanaka, et al., J. Mater. Chem. 2 (1992) 703–707.
[41] G. Lei, Z. Dai, Z. Fan, et al., Carbon 155 (2019) 204–214.
[42] X. Zheng, Y. Li, L. Zhang, et al., Appl. Catal. B: Environ. 252 (2019) 98–110.
[43] X. Zheng, L. Shen, X. Chen, et al., Inorg. Chem. 57 (2018) 10081–10089.
[44] F. Zhang, X. Zhang, Z. Hao, et al., J. Hazard. Mater. 342 (2018) 749–757.
[45] Q. Sun, X. Xu, H. Peng, et al., Chinese J. Catal. 37 (2016) 1293–1302.
[46] Y. Xia, W. Zhan, Y. Guo, et al., Chinese J. Catal. 37 (2016) 2069–2078.
[47] S. Singh, Bull. Mater. Sci. 27 (2004) 537–541.
[48] C. Liu, H. Xian, Z. Jiang, et al., Appl. Catal. B: Environ. 176 (2015) 542–552.
[49] X. Zheng, Y. Li, Y. Zheng, et al., ACS Catal. 10 (2020) 3968–3983.
[50] Z. Lu, D. Ma, L. Yang, et al., Phys. Chem. Chem. Phys. 16 (2014) 12488–12494.
[51] S. Li, Q. Gu, N. Cao, et al., J. Mater. Chem. A Mater. Energy Sustain. 8 (2020) 8892–8902.
[52] L. Shen, X. Zheng, G. Lei, et al., Chem. Eng. J. 346 (2018) 238–248.
[53] M.V. Vaishampayan, R.G. Deshmukh, P. Walke, I. Mulla, Mater. Chem. Phys. 109 (2008) 230–234.
[54] X. Zheng, Y. Li, S. Liang, et al., J. Catal. 389 (2020) 382–399.